Supplement of Atmos. Meas. Tech., 13, 6271–6292, 2020
https://doi.org/10.5194/amt-13-6271-2020-supplement

Atmospheric Measurement Techniques
Open Access

Supplement of

An improved TROPOMI tropospheric HCHO retrieval over China

Wenjing Su et al.

Correspondence to: Cheng Liu (chliu81@ustc.edu.cn) and Ka Lok Chan (ka.chan@dlr.de)

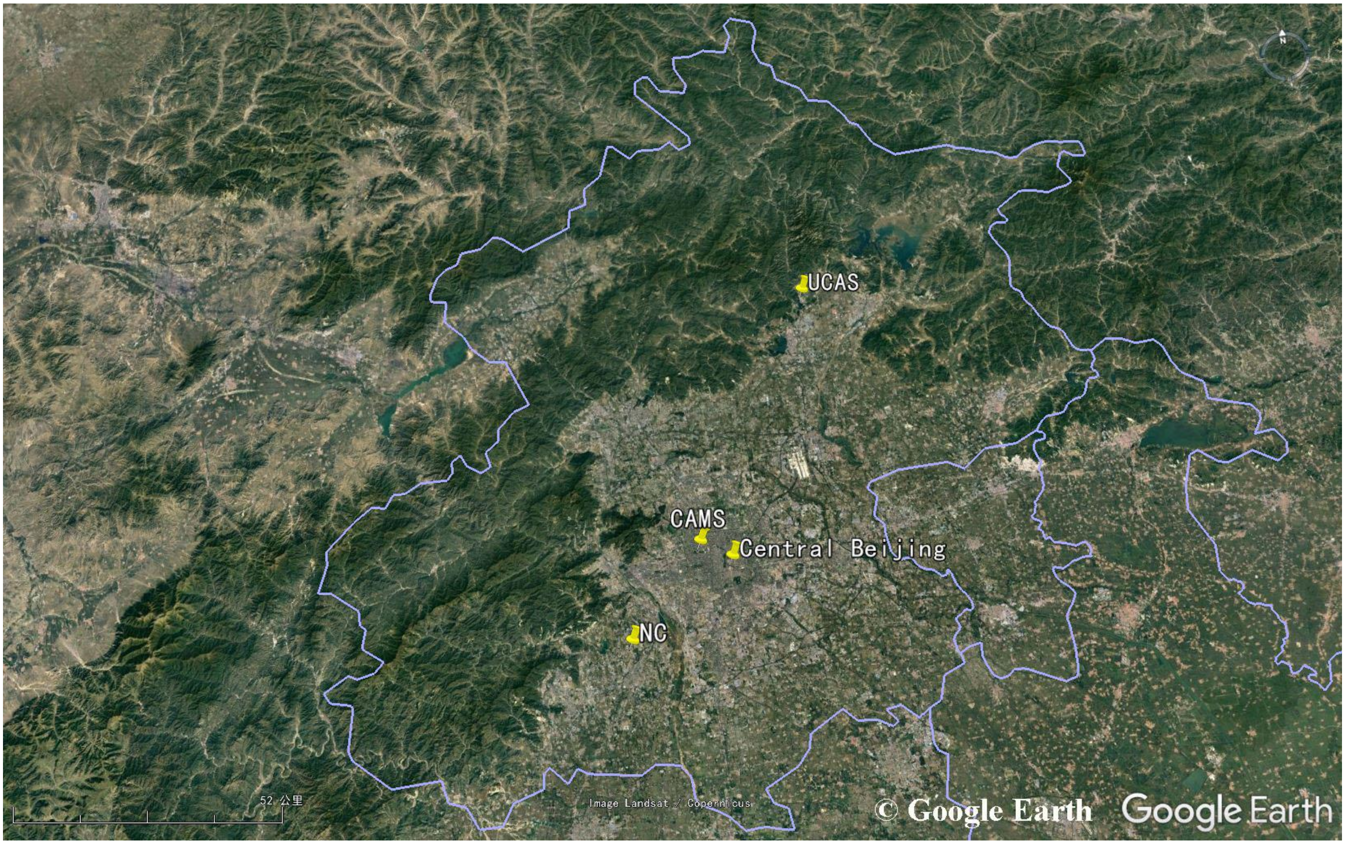

Figure S1. Locations of three MAX-DOAS sites in Beijing

Table S1. The DOAS retrieval settings for MAX-DOAS HCHO SCD.

Fitting window	322.5-358 nm
polynomial	5rd order
Solar reference spectrum	(Chance and Kurucz, 2010)
HCHO cross sections	(Meller and Moortgat, 2000), 297K
O_3 cross sections[(a)]	(Serdyuchenko et al., 2014), 223 and 243K
NO_2 cross sections[(b)]	(Vandaele et al., 1998) , 298K
BrO cross sections	(Fleischmann et al., 2004), 223K
O_4 cross section	(Thalman and Volkamer, 2013) , 293K
Molecular ring	

[(a)] I_0 correction was applied using a SCD of 10^{20} molec cm^{-2}

[(b)] I_0 correction was applied using a SCD of 10^{17} molec cm^{-2}

The TROPOMI Calibration Key Data (CKD) contains slit function for the UV, UVIS, NIR and SWIR detector bands derived from TROPOMI calibration measurements performed in March 2015 at CSL in Liege. The preflight instrument slit function are available at http://www.tropomi.eu/data-products/isrf-dataset. To estimate the stability of TROPOMI slit function, the Full-Width at Half-Maximum (FWHM) and asymmetric factor are obtained by fitting daily irradiance and the high resolution solar spectra Non-linearly assuming the asymmetric Gaussian shape of slit function (shown in Fig. S1). The online fitted slit functions match well with the TROPOMI preflight measurements except for a large difference in the tail of slit function. It may be caused by not considering wavelength dependence in slit function fitting. The FWHMs vary little and decreased 0.00014 for row 1 and 0.00028 for row 450. The asymmetric factors vary larger than FWHM while the range of variation is within 0.007 for row 1 and row 450. The results show that the TROPOMI slit function is stable after lunch.

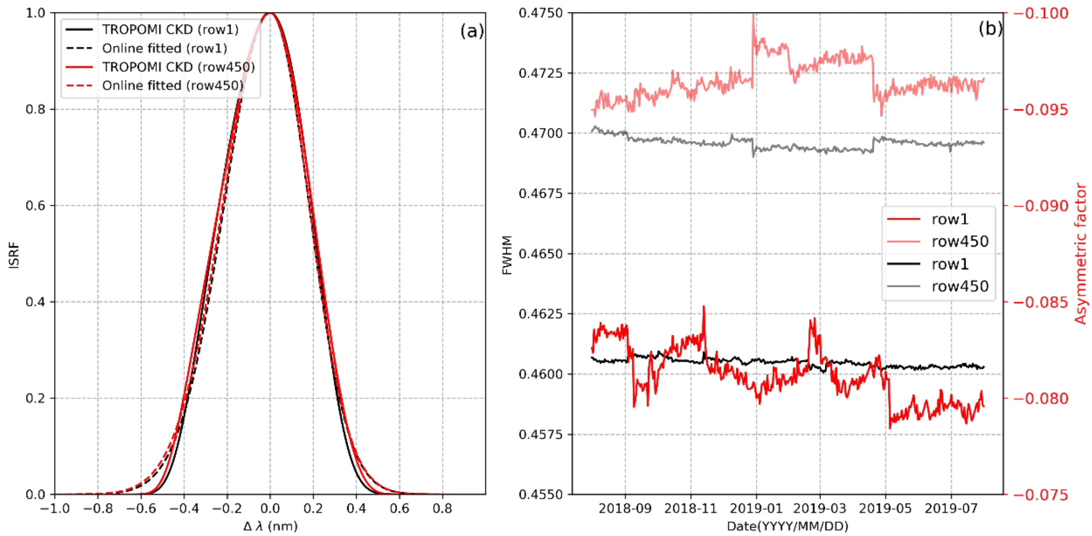

Figure S2. (a) The slit function from TROPOMI CKD at 340nm and online fitted for row 1 and row 450 on 01 August 2018. (b) Time series of FWHM and asymmetric factor of online fitted slit function from August 2018 to July 2019.

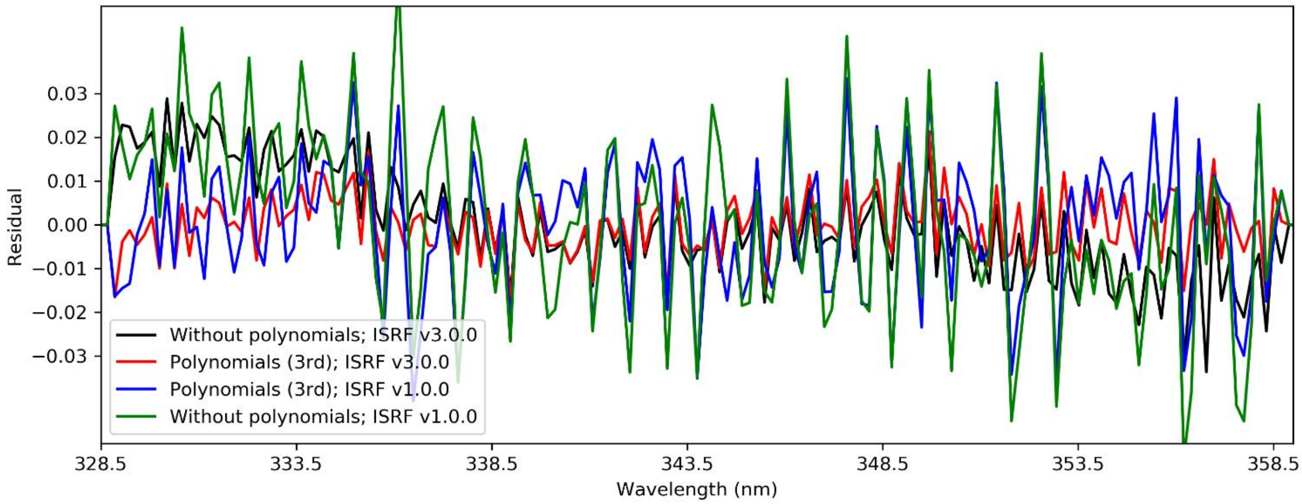

Figure S3. Comparisons of spectral fit residuals using different version of preflight slit function and using different polynomials during wavelength calibration.

To investigate effects of cross sections on SCD retrieval, we plotted the spectral fitting residual and presented fitting results with considering different cross sections (shown in Figure. S4 and Table S2) on 6 August 2018 over China (orbit 4211). For HCHO polluted case, considering O_3 cross sections at 228K and 295K reduces residual significantly while considering NO_2, BrO and O_4 cross sections affects residual little (Figure. S4 (a)). Moreover, Ring effect and O3 cross sections affect SCD largely and help reduce random error. For HCHO clean case (Figure. S4 (b)), considering NO_2, BrO and O_4 cross sections reduces residual largely. Considering SO_2 cross section in spectral fitting has no contribution on reducing residual and increases residual at some wavelengths on the contrary. New O_3 cross sections have become available in recent years (Serdyuchenko et al., 2014) and wavelength dependence of strong absorber SCD is corrected in (Puķīte et al., 2009), We did the sensitivity test about effect from difference of O_3 cross sections and Taylor series approach on our SCD retrieval for HCHO polluted and clean cases. For HCHO polluted case, using newly published O_3 cross sections changes SCD by 0.7% with random error and RMS unchanged. For HCHO clean case, using newly published O_3 cross sections changes SCD by 1.7% with random error unchanged and RMS increasing 0.1. The SCD difference with and without applying Taylor series approach is 7.1% and 5.98% for HCHO polluted and clean cases, respectively. While applying Taylor series approach increases random error by 1.35% and 6.52% for HCHO polluted and clean cases, respectively.

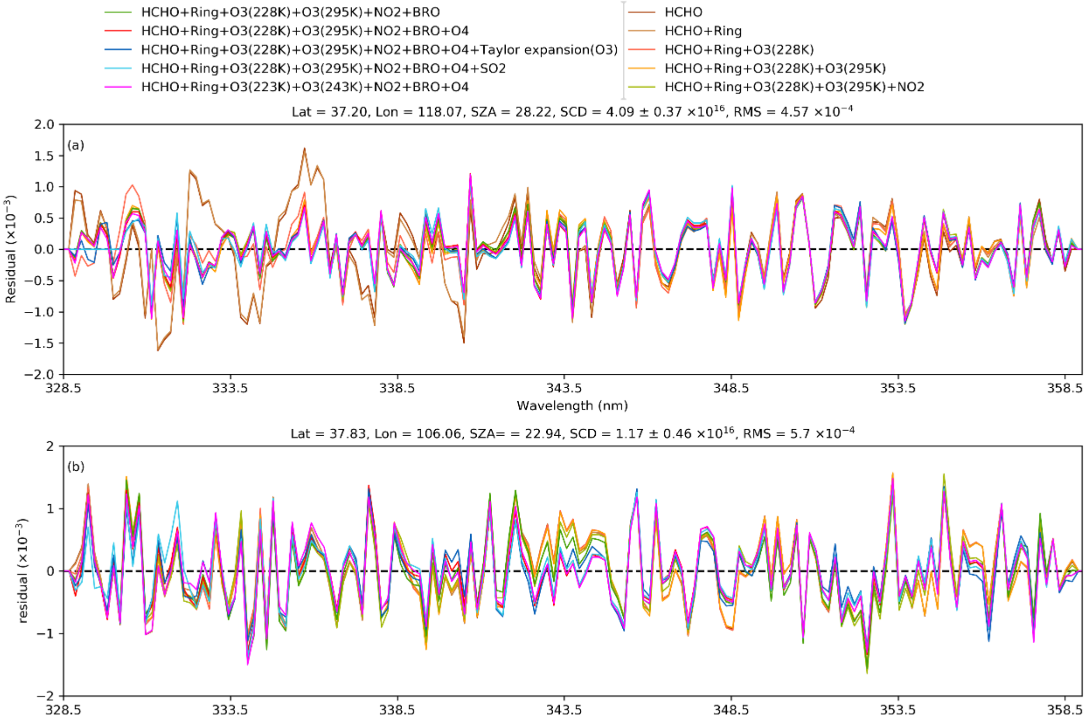

Figure S4. Fitting residuals with considering different cross sections on 6 August 2018 over China for (a) polluted case and (b) clean case. The legend "HCHO" represents only considering HCHO cross section in spectral fitting and the legend "HCHO+Ring+O3(228K)+ O3(295K)+NO2+BRO+O4+Talor expansion(O3)" represents considering all cross sections listed in Table 1 and taking into account the first order Taylor series expansion for O_3 at two temperatures in spectral fitting.

Table S2. The spectral fitting results with considering different cross sections. The unit of DSCD and random error of DSCD is 10^{16} molec cm^{-2} and the RMS is expressed in 10^{-4}

	Polluted case			Clean case		
	DSCD	Random error of DSCD	RMS	DSCD	Random error of DSCD	RMS
HCHO	4.51	0.43	6.3	0.59	0.42	6.3
HCHO+Ring	4.32	0.44	6.3	0.57	0.44	6.3
HCHO+Ring+O_3(228K)	4.27	0.34	4.9	0.57	0.44	6.3
HCHO+Ring+O_3(228K)+O_3(295K)	3.99	0.35	4.7	0.68	0.46	6.3
HCHO+Ring+O_3(228K)+O_3(295K)+NO_2	3.96	0.34	4.6	0.64	0.45	6.1
HCHO+Ring+O_3(228K)+O_3(295K)+BrO	4.09	0.37	4.6	1.15	0.48	6.0
HCHO+Ring+O_3(228K)+O_3(295K)+BrO+O_4	4.09	0.37	4.6	1.17	0.46	5.7
HCHO+Ring+O_3(228K)+O_3(295K)+BrO+O_4	4.38	0.42	4.6	1.10	0.49	5.6

+Taylor expansion (O_3)						
HCHO+Ring+O_3(228K)+O_3(295K)+BrO+O_4 +SO_2	4.40	0.40	4.5	1.73	0.51	5.6
HCHO+Ring+O_3(223K)+O_3(243K)+BrO+O_4	4.12	0.37	4.6	1.19	0.46	5.8

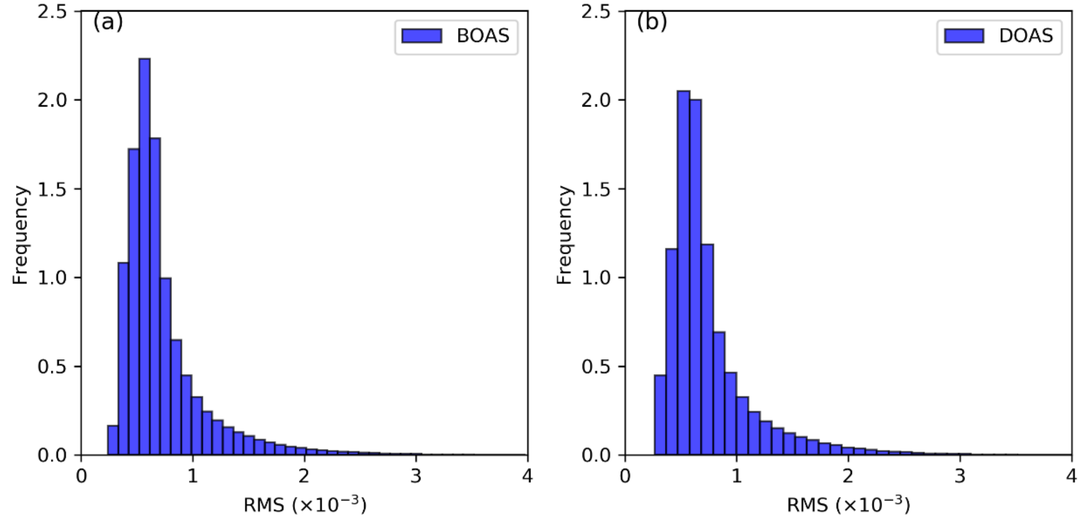

Figure S5. The histograms of the distributions of RMS in our retrieval (a) and operational product retrieval (b)

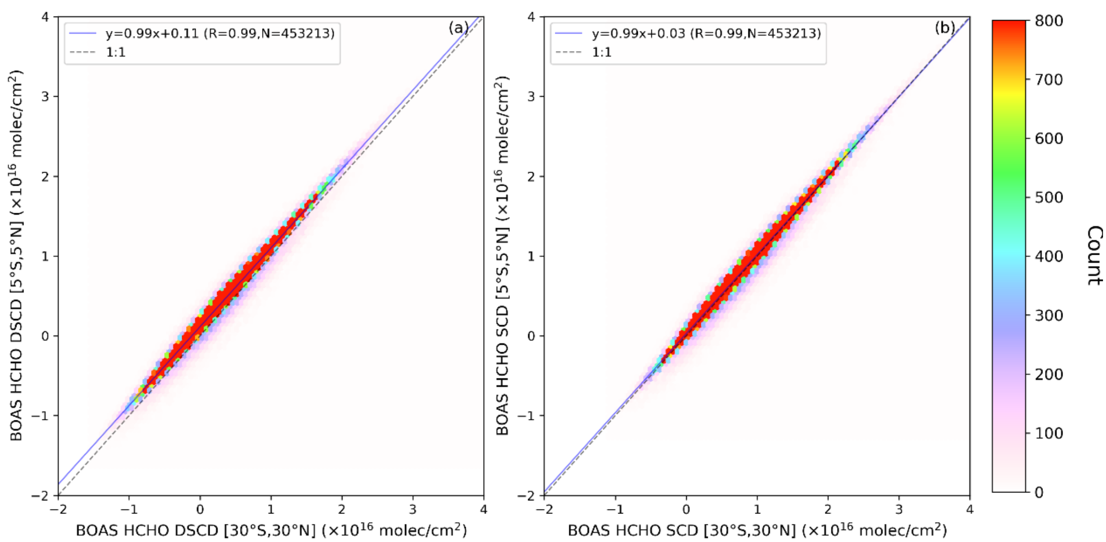

Figure S6. Pixel to pixel comparisons of BOAS HCHO DSCDs (a) and BOAS HCHO SCDs (b) using different earthshine radiance reference on 06 August 2018 in the region between 73° E and 130° E, and 18° N and 54° N. The labels with [30°S, 30°N] represent that average of radiances of the equatorial Pacific (latitude from 30°S to

30°N and longitude from 180°W to 140°W) is used as reference spectra. The labels with [5°S, 5°N] represent that average of radiances of the equatorial Pacific (latitude from 5°S to 5°N and longitude from 180°W to 120°W) is used as reference spectra.

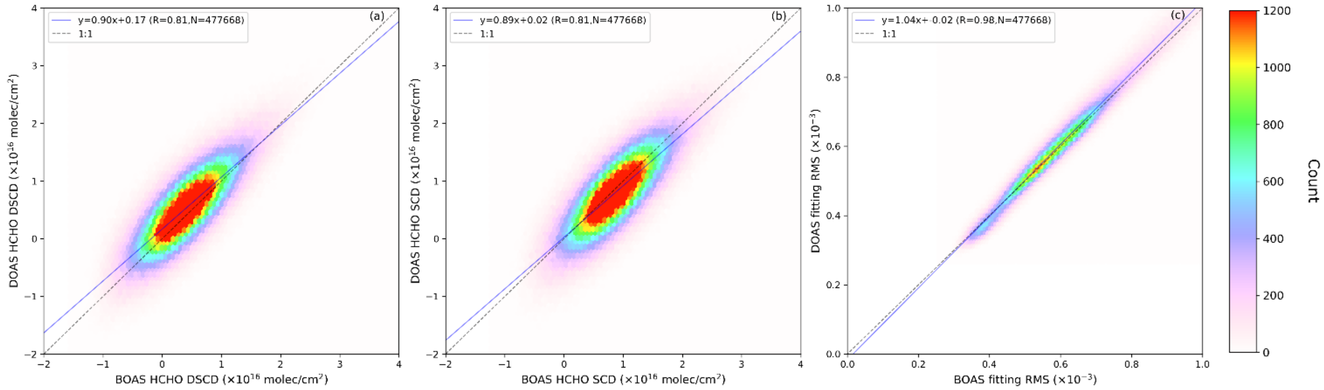

Figure. S7. (a) Pixel to pixel comparisons of DOAS and BOAS HCHO DSCDs, (b) DOAS and BOAS HCHO SCDs and (c) DOAS and BOAS fitting RMS on 06 August 2018 in the region between 73° E and 130° E, and 18° N and 54° N. Same retrieval settings are used in DOAS and BOAS retrieval.

Table S3. The seasonal and annual average HCHO VCD in provincial-level administrative region of China (Unit: 10^{16} molec cm^{-2})

Provincial administrative regions of China	autumn 2018	winter 2018	spring 2019	summer 2019	annual average
Tianjin	**1.32**	**1.16**	**1.26**	**2.10**	**1.46**
Shandong	1.20	1.09	1.17	1.72	1.29
Beijing	1.11	0.98	1.14	1.91	1.29
Jiangsu	1.15	1.17	1.21	1.59	1.28
Anhui	1.14	1.22	1.16	1.51	1.26
Shanghai	1.22	1.20	1.19	1.34	1.24
Henan	1.11	1.15	1.12	1.56	1.23
Hong Kong	1.31	1.19	1.02	1.22	1.19
Hebei	1.05	0.96	1.06	1.62	1.17
Zhejiang	1.16	0.93	1.12	1.32	1.13
Hubei	0.96	1.09	1.06	1.34	1.12
Guangdong	1.08	1.06	1.04	1.21	1.10

Jiangxi	1.03	0.94	1.05	1.29	1.08
Hunan	0.98	0.98	1.06	1.25	1.06
Liaoning	0.97	0.83	1.01	1.43	1.06
Guangxi	0.96	1.00	1.14	1.14	1.06
Hainan	0.89	0.97	1.16	1.15	1.04
Macao	1.23	1.00	0.92	0.87	1.01
Chongqing	0.81	0.96	1.03	1.21	1.00
Shanxi	0.82	0.83	0.96	1.34	0.99
Fujian	0.95	0.91	0.96	1.13	0.99
Shaanxi	0.79	0.86	0.92	1.22	0.95
Jilin	0.88	0.77	0.96	1.16	0.94
Guizhou	0.70	0.94	1.09	0.94	0.92
Taiwan	0.85	0.87	0.91	0.94	0.89
Heilongjiang	0.83	0.76	0.83	1.00	0.85
Ningxia Hui	0.75	0.79	0.79	1.05	0.85
Yunnan	0.68	0.87	0.96	0.83	0.84
Sichuan	0.66	0.84	0.85	0.90	0.81
Nei Mongol	0.75	0.58	0.71	1.02	0.77
Xinjiang Uygur	0.72	0.58	0.67	0.85	0.71
Gansu	0.64	0.64	0.69	0.86	0.70
Tibet	0.52	0.46	0.54	0.62	0.53
Qinghai	0.45	0.48	0.52	0.65	0.53
National average	**0.93**	**0.91**	**0.98**	**1.21**	**1.01**

References

Chance, K., and Kurucz, R. L.: An improved high-resolution solar reference spectrum for earth's atmosphere measurements in the ultraviolet, visible, and near infrared, Journal of quantitative spectroscopy and radiative transfer, 111, 1289-1295, https://doi.org/10.1016/j.jqsrt.2010.01.036, 2010.

Fleischmann, O. C., Hartmann, M., Burrows, J. P., and Orphal, J.: New ultraviolet absorption cross-sections of BrO at atmospheric temperatures measured by time-windowing Fourier transform spectroscopy, Journal of Photochemistry and Photobiology A: Chemistry, 168, 117-132, https://doi.org/10.1016/j.jphotochem.2004.03.026, 2004.

Meller, R., and Moortgat, G. K.: Temperature dependence of the absorption cross sections of formaldehyde between 223 and 323 K in the wavelength range 225–375 nm, Journal of Geophysical Research: Atmospheres, 105, 7089-7101, https://doi.org/10.1029/1999JD901074, 2000.

Puķīte, J., Kuhl, S., Deutschmann, T., Platt, U., and Wagner, T.: Extending differential optical absorption spectroscopy for limb measurements in the UV, Atmos. Meas. Tech., 3, 631-653, 2009.

Serdyuchenko, A., Gorshelev, V., Weber, M., Chehade, W., and Burrows, J.: High spectral resolution ozone absorption cross-sections–Part 2: Temperature dependence, Atmos. Meas. Tech., 7, 625-636, https://doi.org/10.5194/amt-7-625-2014, 2014.

Thalman, R., and Volkamer, R.: Temperature dependent absorption cross-sections of O 2–O 2 collision pairs between 340 and 630 nm and at atmospherically relevant pressure, Phys Chem Chem Phys, 15, 15371-15381, https://doi.org/versity o, 2013.

Vandaele, A. C., Hermans, C., Simon, P. C., Carleer, M., Colin, R., Fally, S., Merienne, M.-F., Jenouvrier, A., and Coquart, B.: Measurements of the NO2 absorption cross-section from 42 000 cm− 1 to 10 000 cm− 1 (238–1000 nm) at 220 K and 294 K, Journal of Quantitative Spectroscopy and Radiative Transfer, 59, 171-184, https://doi.org/10.1016/S0022-4073(97)00168-4, 1998.